https://doi.org/10.5194/egusphere-2026-1728
Preprint. Discussion started: 18 May 2026

Complexation strength between organic carbon and transition metal ions dominates the photochemical conversion of SO_2 to sulfates

Shaojie Yang, Shiwei Lai, Jianwei Zheng, Hao Na, Fu Li, Wangjin Yang, Chong Han
School of Metallurgy, Northeastern University, Shenyang, 110819, China
Correspondence: Chong Han (hanch@smm.neu.edu.cn)

Abstract

The photooxidation of SO_2 on organic carbon (OC) is a critical pathway for sulfate formation, yet the role of interactions between OC and transition metal ions (TMIs) in this process remains scarcely understood. We systematically investigated potential influences of TMIs (Fe^{3+}, Cu^{2+} and Mn^{2+}) on the conversion of SO_2 to sulfates on OC from coal combustion under irradiation. Fe^{3+} exhibited a significantly antagonistic effect, whereas Cu^{2+} and Mn^{2+} enhanced SO_2 uptake and sulfate generation on OC. Spectroscopic evidences, including absorbance decreasing and fluorescence quenching, confirmed the complexes formation of TMI with chromophores in OC. Fe^{3+} owned the strongest binding affinity with chromophores, followed by Cu^{2+} and Mn^{2+}. This variation in the coordination strength dominated the generation of reactive species, such as free electrons (e^-), superoxide radicals ($•O_2^-$), H_2O_2 and hydroxyl radicals (•OH), and •OH acted as a pivotal trigger to drive the sulfate production. Extended investigations containing more metal ions demonstrated that the regulatory effects on the sulfate production were generally governed through their ability to suppress or facilitate the •OH generation.

Graphical abstract:

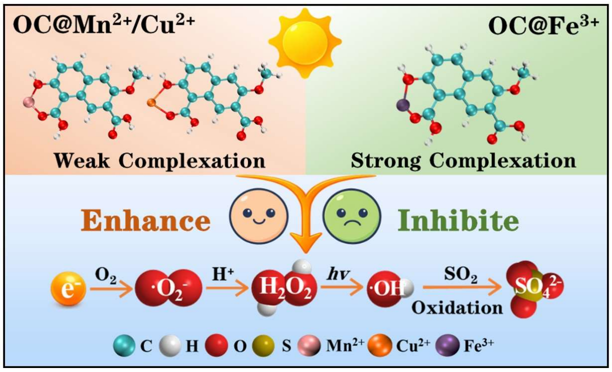

1 Introduction

Fine particulate matter ($PM_{2.5}$) is a complex mixture of inorganic and organic species, and plays a central role in the persistent haze events (Fan et al., 2016; Huang et al., 2014; Peng et al., 2021). The rapid accumulation of sulfates in $PM_{2.5}$ significantly influences atmospheric radiative forcing, air quality and human health (Zhang et al., 2020a; Salana et al., 2024). Sulfates primarily stem from SO_2 oxidation, including reactions with hydroxyl radicals (•OH) in the gas phase and aqueous oxidation in cloud and fog droplets involving various oxidizing species (Tsona and Du, 2019; Liu et al., 2020a; Jiang et al., 2009; Hoyle et al., 2016; Liu and Abbatt, 2021). However, only considering these pathways usually leads to a pronounced gap between the modeled and observed sulfate concentrations during the haze events (Li et al., 2017; Eckhardt et al., 2015; Zheng et al., 2015).

To bridge this gap, several heterogeneous pathways have been proposed, involving reactions of SO_2 on $PM_{2.5}$, mineral dust (e.g., Arizona test dust and metal oxides), inorganic salt (e.g., nitrates and NaCl), soot and organic aerosols (Zhang et al., 2020c; Zhang et al., 2019; Dupart et al., 2012; Yang et al., 2024a; Cao et al., 2024b; Zhang et al., 2022). Although these heterogeneous reactions have narrowed the discrepancies between model prediction and field observation concentrations of sulfates, substantial uncertainties and controversies still remain (Wang et al., 2014). This may be attributed to the fact that most studies mainly focus on simplified single-component systems and overlook the extreme complexity of multicomponent aerosols under realistic atmospheric conditions. Recent evidence highlighted that the potential interactions among distinct components in aerosols can significantly influence the transformation pathways of atmospheric pollutants (Zhang and Chan, 2023; Zhang et al., 2023). For instance, organic carbon (OC) in soot can donate electrons to elemental carbon (EC) and enhance the electron-hole separation under irradiation, thereby generating more •OH and promoting the conversion of SO_2 to sulfates (Zhu et al., 2022). OC-derived photosensitizers activated both O_2 and Cl^- in NaCl-OC under ultraviolet light, producing •OH and Cl• that synergistically oxidized SO_2 to sulfates (Tang et al., 2023).

OC from coal combustion can serve as a photosensitive electron donor under irradiation, initiating the formation of reactive oxygen species (ROS), which subsequently oxidized SO_2 to sulfates (Yang et al., 2025). In atmospheric aerosols, OC often coexisted with various TMIs, especially in some regions influenced by the combustion, vehicular emissions, and industrial processes (Yang et al., 2024b; Deng et al., 2022; Zhang et al., 2020b; Shiraiwa et al., 2017; Hua et al., 2025). This coexistence was not a simple superposition of their specific roles. OC usually contained diverse functional groups such as carboxyl, hydroxyl, and carbonyl moieties, which can interact with TMIs via the complexation, metal-proton ion exchange and electrostatic adsorption, forming organometallic complexes in aerosols (Li et al., 2022; Wang et al., 2021c; Wang et al., 2021b). Furthermore, the binding strength between OC and TMIs varied with the specific type of TMIs, which was related to the differences in ionic radius, oxidation state, and electronic configuration that influenced coordination chemistry and redox reactivity (Wang et al., 2021a; Pan et al., 2020). These interactions were expected to exert antagonistic or synergistic effects on the ROS formation (Li et al., 2022; Pan et al., 2020; Wan et al., 2019; Lu et al., 2019). The potential roles of OC and TMIs interactions in the heterogeneous photochemical oxidation of SO_2 haven't been systematically investigated, which may restrict the exact incorporation of OC photochemistry into the sulfate formation prediction models.

Our previous work mainly focused on the intrinsic photo-reactivity of OC and its dependence on the physicochemical properties (Yang et al., 2025). In this study, laboratory experiments and theoretical calculations were conducted to elucidate the influences of TMIs (Fe^{3+}, Mn^{2+} and Cu^{2+}) on the photooxidation of SO_2 to sulfates on OC from coal combustion. Differences in the photochemical activity were quantified by measuring SO_2 uptake coefficients and sulfate yields.

https://doi.org/10.5194/egusphere-2026-1728
Preprint. Discussion started: 18 May 2026

Changes in the optical properties were examined to evaluate the potential interactions between OC and TMIs. Mechanism insights into the reactive species generation, including e^-, $\bullet O_2^-$, H_2O_2 and $\bullet OH$, clarified how these interactions regulated the SO_2 photooxidation. Finally, further investigation involving multiple metal ions commonly within atmospheric aerosols highlighted the broader significance of OC and TMIs interactions in the sulfate formation.

2 Materials and methods

2.1 Preparation of OC and OC@TMIs samples

As shown in Fig. S1, OC was obtained with a custom combustion and sampling apparatus. The coal in the combustion experiment originated from Shanxi Province, China. The details of OC sampling and preparation are provided in Text S1. 1 mL of the extracted OC solution was dropped onto 6.0 × 1.5 cm prebaked quartz-fiber filters, and the solvents were dried under a N_2 stream (100 mL min^{-1}) in the dark at 298 K. Then, the organic carbon content was measured to be 818.4 ± 53.0 µgC mL^{-1} using a total organic carbon analyzer (TOC-5000 RD, Metash).

The sources and purities of salt chlorides used here are provided in Text S2. Stock solutions of metal salts (1.5 mM, in ultrapure water) were mixed with the OC solution at a 1:2 volume ratio, yielding mixtures containing 0.5 mM metal ions and 545.6 ± 35.3 µgC mL^{-1} (Fig. S1). This metal-ion concentration was close to the levels reported in heavily polluted atmospheric conditions.(Li et al., 2022) Each mixture was ultrasonicated for 30 min at 25 ℃ in the dark. The resulting products were designated as OC@TMI, where OC@TMI referred to a series of samples prepared with different TMIs (e.g., OC@Fe^{3+}, OC@Cu^{2+} and OC@Mn^{2+}). 1.5 mL of the mixed solution was deposited on the inner surface of a quartz flow tube (20 cm length, 1.0 cm inner diameter). The flow tube was rotated slowly to ensure the uniform wetting of the surface. The coating was obtained by drying the samples under a N_2 stream (100 mL min^{-1}) in the dark environment at 298 K to prevent photochemical interference.

2.2 Flow tube experiments and SO_2 uptake coefficients

The SO_2 uptake experiments were performed at ambient pressure in a horizontal cylindrical quartz flow tube reactor (34 cm length, 1.6 cm i.d.), as shown in Fig.S1. The details of the flow reactor and reaction procedure are given in Text S3. The changes in the SO_2 concentration were measured with a SO_2 analyzer (Thermo 43i). The calculation of the SO_2 uptake coefficient is

https://doi.org/10.5194/egusphere-2026-1728
Preprint. Discussion started: 18 May 2026

described in Text S4.

2.3 Analysis methods

2.3.1 Measurements of sulfate products

The functional group changes during the photochemical reaction of SO_2 on the samples were characterized using in situ attenuated total reflection infrared (ATR-IR) spectroscopy (Nicolet iS50, Thermo Scientific), which equipped with a mercury-cadmium-telluride (MCT) detector. Descriptions of experimental process are given in Text S5.

The sulfate ions were quantified using an ion chromatography (IC) system (CIC-D120+, Shenghan) with an analytical column (AS11-HC, Thermo) and a conductivity detector. The testing procedures are described in Text S6.

2.3.2 Optical property measurements

The optical properties of OC, TMIs, and OC@TMIs were analyzed using the UV-visible absorption spectroscopy and the excitation-emission matrix (EEM) fluorescence spectroscopy. The UV-visible spectra were recorded by the UV-visible spectrophotometer (UV-2550, Shimadzu) with a 1.0 cm pathlength cell in the wavelength range of 200−600 nm. A mixed solution of methanol and water (2:1, v/v) was used as the blank background.

The EEM fluorescence spectroscopy were measured via a fluorescence spectrophotometer (FP8550, Jasco) at 700 V voltage and 3-D mode in the wavelength ranges of 200−400 nm for excitation (Ex.) and 300−520 nm for emission (Em.). The fluorescence spectra were recorded at 5 nm intervals and a scan speed of 2400 nm min^{-1} in a 1 cm path-length quartz cuvette. Samples were diluted to one-fifteenth of the original concentrations to minimize the inner-filter effect (IFE) and reabsorption artifacts, which can distort the excitation−emission spectra at high sample concentrations. Instrument calibration, correction for inner-filter effects and normalization of fluorescence intensity to the Raman units (RU) of solvent were conducted before EEM spectral analysis. The EEM data were modeled with the parallel factor analysis (PARAFAC) through the DOMFluo toolbox (version 0.2.0) for MATLAB. Based on the evaluation of 2−4 components using EEM profiles and residual error patterns, a 3-component model was ultimately selected (Fig. S4).

2.3.3 Electrochemical measurements

The electron donating capacities (EDC) of the samples were determined using an electrochemical workstation (CHI760F, Shanghai Chenhua Co., Ltd.) equipped with a three-electrode system. The testing procedures are described in Text S7. The EDC was calculated as the following Eq. (1) (Ma et al., 2024),

$$\mathrm{EDC} = \frac{\int \frac{I_{ox}}{F} d_t}{m_{\text{organic carbon}}} \quad (1)$$

where I_{ox} means the OC oxidation curves; F is the constant of Faraday, which is equal to 96485 s A mol^{-1} e^{-}; $m_{\text{organic carbon}}$ represents the amount of organic carbon of samples.

2.3.4 EPR measurements

Reactive oxygen species (ROS) under irradiation were analyzed using an electron paramagnetic resonance spectrometer (A300, Bruker). For the radical detection, 20 μL of 0.05 M DMPO (in methanol) and BMPO (in water) were used as spin traps for superoxide radicals ($\bullet O_2^-$) and •OH, respectively. The instrument parameters were set as follows: magnetic field range of 3450–3550 G, central field range of 3500 G, scan time of 30 s and microwave power of 20 mW.

2.3.5 H_2O_2 detection

The H_2O_2 generation was analyzed by the $TiOSO_4$ colorimetric method (Liu et al., 2023; Li et al., 2023). $TiOSO_4$ reacted with H_2O_2 to form a yellow titanium-peroxide complex ($Ti(IV)O_2^{2+}$), which exhibited a characteristic absorbance peak at 405 nm. The H_2O_2 concentration was determined using the H_2O_2 standard curve (Fig. S5), and the testing procedure is given in Text S8.

2.3.6 X-ray photoelectron spectroscopy

The X-ray photoelectron spectroscopy (XPS, ESCALAB 250Xi, Thermo) was employed to investigate the valence state variations of metal ions under irradiation. Fresh samples (3 mL, prepared by 2 mL OC extraction with 1 mL ionic solution) or the ones photoaged by SO_2 were combined with SiO_2 (100 mg) and dried by rotary evaporation under ultra-high vacuum conditions (10^{-9} mbar). For XPS analysis, aluminum Kα radiation ($h\nu$ = 1486.68 eV, spot size 500 μm) was used as the excitation source. The instrument was operated at 15 kV and 10 mA. Signals were accumulated over 5−10 scans, and the spectra were recorded with a pass energy of 30 eV and a step size of 0.05 eV. Peak deconvolution was conducted to resolve the contributions of different valence states.

https://doi.org/10.5194/egusphere-2026-1728
Preprint. Discussion started: 18 May 2026

2.3.7 Density functional theory calculations

Density functional theory (DFT) calculations were carried out through the quantum chemistry software Gaussian 16. Geometry optimizations and energy calculations were conducted at the B3LYP/LANL2DZ level and B3LYP-D3/def2-TZVP level, respectively. O_2 adsorption on OC and the corresponding IGMH diagrams were analyzed using Multiwfn (Lu and Chen, 2011; Lu, 2024). The calculation about the complexation energy of OC with TMIs and O_2 adsorption energy are described in Text S9.

3 Results and discussion

3.1 Dependence of SO_2 uptake on metal ions

Fig. 1a–c illustrates the temporal evolution of SO_2 concentration on OC, TMIs and OC@TMIs under irradiation. Here, the SO_2 signal for OC+TMIs represented the arithmetic sum of the SO_2 uptake measured for OC and TMIs in the separate experiments. All errors denoted the standard deviations of three independent replicates. Because chloride salts were used here, OC@NaCl control experiments were conducted. The decreasing trend of SO_2 concentration on OC@NaCl was the same as that on OC, suggesting no measurable effect of Cl^- on the SO_2 uptake (Fig. S6). The SO_2 loss on $FeCl_3$ or $MnCl_2$ was less than that on OC, while it was similar for $CuCl_2$ and OC. When SO_2 was exposed to OC@Fe^{3+}, the SO_2 concentration decreased by 1–2 ppb, which was obviously lower than that for OC+Fe^{3+}. This indicates that the coexistence of Fe^{3+} with OC markedly suppressed the photochemical uptake of SO_2. The SO_2 loss on OC@Cu^{2+} and OC@Mn^{2+} was markedly greater than that on OC+Cu^{2+} and OC+Mn^{2+}, respectively. This suggests that both Cu^{2+} and Mn^{2+} enhanced the photochemical reaction of SO_2 with OC.

The initial (γ_i) and steady-state (γ_{ss}) uptake coefficients of SO_2 are summarized in Fig. 1d. To better quantify TMIs effects, the uptake coefficient for OC+TMIs was calculated using the SO_2 uptake amount for OC+TMIs as the reference. The γ_{ss} was consistently lower than the γ_i due to the gradual aging and the depletion of photoactive components during the reaction. The γ_{ss} on OC@Fe^{3+} only accounted for 5% of that on OC+Fe^{3+}, confirming that Fe^{3+} significantly restrained the photochemical SO_2 uptake on OC. In contrast, γ_{ss} for OC@Cu^{2+} and OC@Mn^{2+} was 1.83 and 2.93 times of the corresponding one for OC+Cu^{2+} and OC+Mn^{2+}, respectively.

This definitely suggests that the coexistence of Cu^{2+} and Mn^{2+} with OC has synergistic effects on the photochemical uptake of SO_2, with Mn^{2+} exhibiting a stronger enhancement than Cu^{2+}. Overall, these contrasting behaviors reveal that the addition of TMIs to OC can either restrict (Fe^{3+}) or facilitate (Cu^{2+} and Mn^{2+}) the photochemical uptake of SO_2, highlighting the distinct roles of TMIs in modulating the OC reactivity.

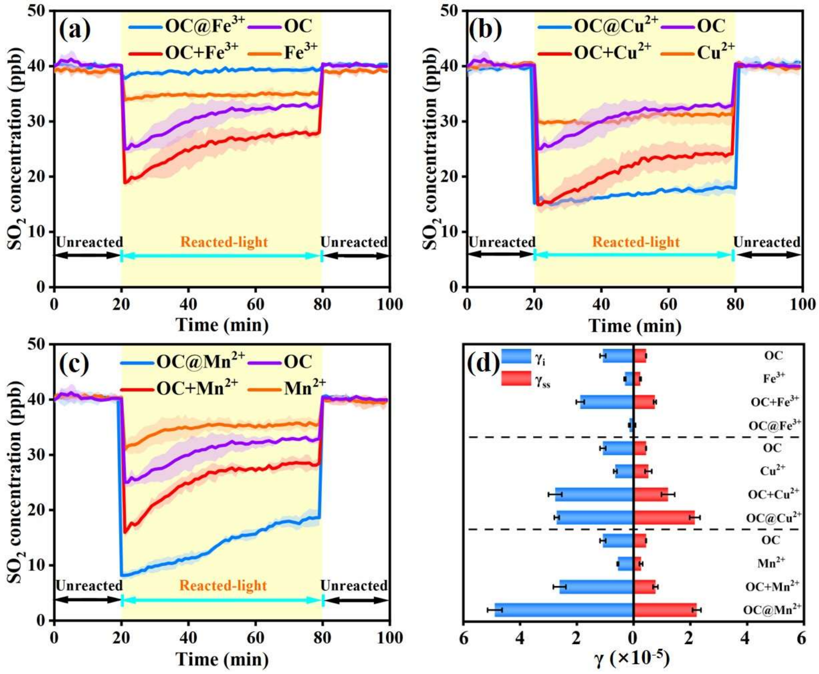

Figure 1. (a–c) Temporal variations of the SO_2 concentration during the heterogeneous reaction of SO_2 with OC, TMIs, OC+TMIs and OC@TMIs under irradiation. (OC+TMIs denoted the arithmetic sum of the SO_2 uptake measured for OC and TMIs in the separate experiments). (d) Initial uptake coefficients (γ_i) and steady-state uptake coefficients (γ_{ss}) of SO_2 under irradiation. Reaction conditions: irradiance of 1.05×10^{16} photons cm^{-2} s^{-1}, 40 ppb SO_2, 298 K and 60% RH.

3.2 Dependence of sulfate formation on metal ions

The contour maps of in-situ ATR-IR spectra of OC, TMIs and OC@TMIs exposed to SO_2 under irradiation are displayed in Fig. 2a. Several characteristic sulfate (SO_4^{2-} or HSO_4^-) bands were identified for all samples in the 1300–1000 cm^{-1} region (Zhang et al., 2023; Zhang et al., 2019). It was noted that these bands intensified progressively with the time, reflecting the continuous accumulation of sulfates.

The IC results provided quantitative evidence of sulfate formation under irradiation (Fig. 2b). For OC@Fe^{3+}, sulfate production was much lower than that on OC or FeCl$_3$. Specifically, the sulfate mass on OC@Fe^{3+} was merely 18% of that for OC+Fe^{3+}, confirming that Fe^{3+} restrained the formation of sulfates on OC. In contrast, the sulfate mass on OC@Cu^{2+} and OC@Mn^{2+} was 1.08 and 1.36 times larger than that for OC+Cu^{2+} and OC+Mn^{2+}, respectively. These confirm that both Cu^{2+} and Mn^{2+} promote the photochemical oxidation of SO$_2$ to sulfates on OC. Taken together with the SO$_2$ uptake data in Fig.1, TMIs exerted markedly different influences on SO$_2$ conversion to sulfates on OC.

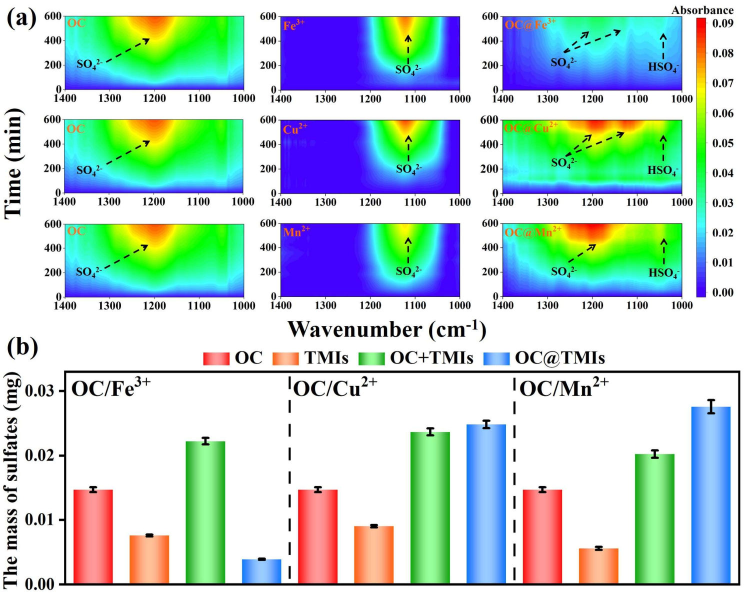

Figure 2. (a) Contour map of in-situ ATR-IR spectra of OC, FeCl$_3$, CuCl$_2$, MnCl$_2$, OC@Fe^{3+}, OC@Cu^{2+} and OC@Mn^{2+} exposed to SO$_2$ under irradiation. Reaction conditions: irradiance of 7.40×10^{15} photons cm^{-2} s^{-1}, 2 ppm SO$_2$, 298 K and 60% RH. (b) Mass of sulfates produced on OC, TMIs, OC+TMIs and OC@TMIs after the 10 h reaction with SO$_2$ under irradiation (OC+TMIs denoted the arithmetic sum of the mass of sulfates measured for OC and TMIs in the separate experiments). Reaction conditions: irradiance of 1.05×10^{16} photons cm^{-2} s^{-1}, 200 ppb SO$_2$, 298 K and 60% RH.

https://doi.org/10.5194/egusphere-2026-1728
Preprint. Discussion started: 18 May 2026

3.3 Spectroscopic evidence for complexation between OC and TMIs

The complexation between OC and TMIs may occur and alter the optical properties of OC (Wang et al., 2024). Changes in optical absorption and steady-state fluorescence signals were used to probe these interactions. Fig. S7a−c display the UV-vis spectra of OC, TMIs, OC+TMIs and OC@TMIs. The absorbance for OC+TMIs was defined as the arithmetic sum of the absorbance measured separately for OC and TMIs. OC and OC@TMIs exhibited a sharp increase in the absorbance at the shorter wavelengths. $FeCl_3$, $CuCl_2$ and $MnCl_2$ owned very weak absorbance. OC@Fe^{3+}, OC@Cu^{2+} and OC@Mn^{2+} presented lower absorbance than OC+Fe^{3+}, OC+Cu^{2+} and OC+Mn^{2+}, respectively, which can be attributed to the complexation between OC and TMIs (Li et al., 2022). The FT-IR spectra of OC are displayed in Fig. S8, and the peak assignments are summarized in Table S1. OC contained carboxyl, hydroxyl and carbonyl groups. These oxygen-containing groups with π bonds electrons and lone pairs can served as the complexation sites by donating electrons to the vacant orbitals of TMIs (Wang et al., 2021c). Notably, as shown in Fig. S7d, there was the largest absorbance difference (ΔAbs) between OC@Fe^{3+} and OC+Fe^{3+} in the entire spectral range, indicating the strongest complexation of OC with Fe^{3+} among three TMIs.

EEM fluorescence spectroscopy combining with the PARAFAC analysis were employed to further investigate the complexation interactions between TMIs on OC. Three chromophores are identified in Fig. 3a−c and Fig. S9, and their peak positions and assignments are given in Table S2. C1 (Ex/Em = 265(320)/380 nm) and C2 (Ex/Em = 285(370)/420 nm) were assigned to chromophores with low and high oxidation states, respectively. C3 (Ex/Em = 200(260)/340 nm) belonged to protein-like chromophores (Li et al., 2022; Wang et al., 2021b). Fluorophores at longer emission wavelengths, such as C2, typically owned abundant polar groups, including hydroxyl and carboxyl, which acted as primary binding sites for TMIs (Pan et al., 2020; Lu et al., 2019). The relative contributions of different components to OC shifted upon the addition of TMIs, reflecting the varied complexation strengths of TMIs with OC (Fig. 3d). For OC@Fe^{3+} in comparison with OC, the ratio of C1 obviously increased by 14%, while it decreased by 9% and 5% for C2 and C3, respectively. By contrast, OC@Cu^{2+} and OC@Mn^{2+} showed smaller changes in the C1−C3 proportions. These mean that Fe^{3+} forms the most stable complexes with OC due to its high charge density and trivalent oxidation state, which would enhance the ligand attraction and enable higher coordination numbers (Liu et al., 2022). Cu^{2+} and Mn^{2+}, with lower charge densities and less favorable coordination geometries, exerted weaker complexation effects with OC.

As a comprehensive measure of fluorescence intensity, the total fluorescence volume (TFV) was used to evaluate the overall impact of metal complexations (Fig. 3e). The addition of TMIs led to a reduction in TFV, confirming the fluorescence quenching occurrence. Fe^{3+} caused the most pronounced reduction of TFV (85.2%), followed by Cu^{2+} (13.4%) and Mn^{2+} (1.4%). This strong quenching effect was attributed to the high binding affinity of Fe^{3+} with highly oxidative and protein-like fluorophores. The complexation between OC and TMIs can disrupt the π–π^* conjugation and deactivate fluorescence centers, which contributed to a significant reduction in TFV (Kuramochi et al., 2018). In addition, the complexation of Fe^{3+} with OC could promote the intersystem crossing (ISC) from the singlet state ($^1OC^*$) to the triplet state ($^3OC^*$) (Ruzi et al., 2017; Treacy and Rovis, 2024), enhancing nonradiative decay and further suppressing the fluorescence emission.

To directly demonstrate the complexation strength between TMIs with species in OC, DFT calculations were conducted using phenol (PH), benzoic acid (BA) and a model substance (MS) (Fig. S10). PH and BA were chosen according to FT-IR analysis (Fig. S8), as they represented species with hydroxyl and carboxyl groups commonly presenting in OC. MS simultaneously contained these functional groups with a π-conjugated aromatic backbone to better reflect the structural features of ambient OC. Text S10 and Fig. S11 illustrate the complexation structure of three molecular models with Fe^{3+}, Cu^{2+} and Mn^{2+}. As summarized in Table S3, all molecular models exhibited the highest complexation energy with Fe^{3+}, followed by Cu^{2+} and Mn^{2+}. This was well consistent with the results observed in the UV-Vis and fluorescence spectra.

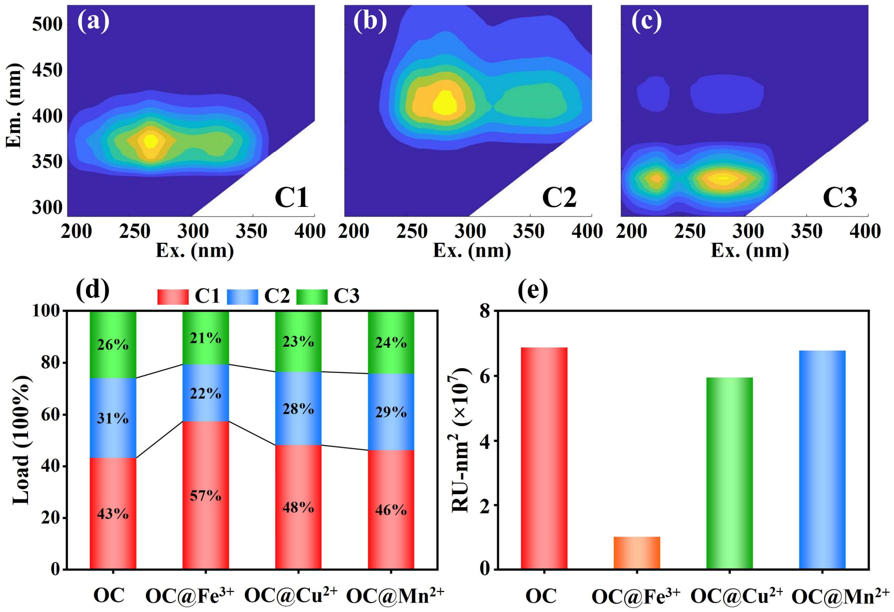

Figure 3. (a−c) Three components extracted by the PARAFAC analysis. (d) Relative fluorescence contributions of C1−C3 in OC, OC@Fe^{3+}, OC@Cu^{2+} and OC@Mn^{2+}. (e) Total fluorescence volume of OC, OC@Fe^{3+}, OC@Cu^{2+} and OC@Mn^{2+}.

3.4 Mechanistic insights into TMIs-regulated oxidation of SO_2 to sulfates

As described through R1−6, previous studies have proposed the photochemical conversion pathways of SO_2 to sulfates on OC (Yang et al., 2025; Yang et al., 2024a). Upon accepting photons, OC is excited to ${}^3OC^*$, which subsequently generates free electrons (R1−2) (Yang et al., 2024a; Wang et al., 2020). These electrons would reduce adsorbed O_2 to $•O_2^-$ (R3) (Zhang et al., 2022). $•O_2^-$ can combine with protons to form hydroperoxyl radicals ($HO_2^•$), which are converted into O_2 and hydrogen peroxides (H_2O_2) (R4) (Zhang et al., 2020c). H_2O_2 undergoes the photolysis to produce •OH (R5), and •OH drives the oxidation of adsorbed SO_2 or H_2SO_3 or HSO_3^- to sulfates (R6) (Liu et al., 2020b).

$$\mathrm{OC} \xrightarrow{hv} {}^3\mathrm{OC}^* \quad \text{(R1)}$$

$$ {}^3\mathrm{OC}^* \rightarrow \mathrm{OC}^+ + e^- \quad \text{(R2)}$$

$$\mathrm{O_2} + e^- \rightarrow \bullet\,\mathrm{O_2^-} \quad \text{(R3)}$$

$$\bullet\,\mathrm{O_2^-} + \mathrm{H^+} \rightarrow \mathrm{HO_2^\bullet} \rightarrow \mathrm{O_2} + \mathrm{H_2O_2} \quad \text{(R4)}$$

$$H_2O_2 \xrightarrow{hv} \bullet OH \quad (R5)$$

$$\bullet OH + SO_2 \text{ or } H_2SO_3\ (HSO_3^-) \rightarrow SO_4^{2-} + H_2O \quad (R6)$$

To verify whether the above mechanism remained operative after the complexation between TMIs and OC, electrochemical and EPR analyses were conducted. Mediated electrochemical oxidation (MEO) data of OC without or with TMIs showed persistent occurrence of the photo-generated electron transfer (Fig. S12 and S13). BMPO was used as the spin-trapping agent. As displayed in Fig. 4a, the characteristic EPR signal of BMPO-•OH adducts was detected under irradiation, confirming the generation of •OH. Moreover, EPR signals of BMPO-•OH adducts followed the order: OC@Mn^{2+} > OC@Cu^{2+} > OC > OC@Fe^{3+}, which well aligned with γ_{ss} and sulfate production. The critical role of •OH in the conversion of SO_2 to sulfates was further determined using $NaHCO_3$ to scavenge •OH (Yang et al., 2024a), where the sulfate formation was markedly restricted (Fig. S14). These demonstrate that •OH generation capacity is the primary determinant of sulfate formation on OC@TMIs.

According to the reactions R1−2, the photogeneration of electrons was an initial step that can affect the reaction activity of OC. Fig. 4b summarizes the distinct regulatory roles of Fe^{3+}, Cu^{2+} and Mn^{2+} in the EDC of OC under irradiation. The EDC of OC@Fe^{3+} (0.00496 μmol e^- (mg C)$^{-1}$) was substantially less than that of OC+Fe^{3+} (0.01904 μmol e^- (mg C)$^{-1}$), suggesting that Fe^{3+} significantly suppressed the photogeneration of electrons. This mainly stemmed from the strong complexation of Fe^{3+} and OC, which masked the redox-active moieties and dynamically quenched $^3OC^*$, restraining free electron formation (Li et al., 2022; Liu et al., 2024).

Fig. 4b shows that EDC of OC@Cu^{2+} (0.02074 μmol e^- (mg C)$^{-1}$) and OC@Mn^{2+} (0.02147 μmol e^- (mg C)$^{-1}$) was higher than that of OC+Cu^{2+} (0.01954 μmol e^- (mg C)$^{-1}$) and OC+Mn^{2+} (0.01811 μmol e^- (mg C)$^{-1}$), respectively. This means that Cu^{2+} and Mn^{2+} enhance the electron-donating ability of OC. These lager EDC may be related to reversible redox cycling of Cu^{2+}/Cu^+ and Mn^{2+}/Mn^{3+} in the photochemical process. In contrast, Fe^{3+} formed more stable complexes with OC that trapped the photogenerated electrons, thereby suppressing efficient redox cycling of Fe^{3+}/Fe^{2+}. Under irradiation, Cu^{2+} was reduced to Cu^+ by accepting photogenerated electrons, which was subsequently re-oxidized to Cu^{2+} by O_2 or electron-deficient functional groups (e.g.,

https://doi.org/10.5194/egusphere-2026-1728
Preprint. Discussion started: 18 May 2026

quinones) (Pan et al., 2020). As displayed in XPS spectra of Cu 2p for OC@Cu^{2+} in Fig. 5a and b, the peaks at 932.5 and 934.3 eV corresponded to Cu^{+} and Cu^{2+}, respectively (Biesinger et al., 2011). The proportion of Cu^{2+}, denoted as R(Cu^{2+}), decreased from 0.67 to 0.59 after photochemical SO_2 aging. This confirms the existence of reversible redox cycling of Cu^{2+}/Cu^{+}. Similarly, Mn^{2+} can be oxidized to Mn^{3+} by photogenerated holes (OC^{+}) or reactive oxygen-containing intermediates on OC, and then Mn^{3+} was reduced by phenolic or aromatic groups on OC (Hansard et al., 2011). The Mn $2p_{3/2}$ spectra of OC@Mn^{2+} exhibited two peaks at 640.4 and 641.9 eV (Fig. 5c and d), which were ascribed to Mn^{2+} and Mn^{3+}, respectively (Xing et al., 2025). The proportion of Mn^{2+} (R(Mn^{2+})) decreased from 0.41 to 0.16 after the reaction, indicating Mn^{2+}/Mn^{3+} redox interconversion. These reversible redox cycles facilitated dynamic interfacial electron transfer by accepting and releasing photogenerated electrons. This bidirectional electron flow can amplify the outward electron flux from OC, thereby increasing the electron-donating capacity (Fulda et al., 2013; Li et al., 2021).

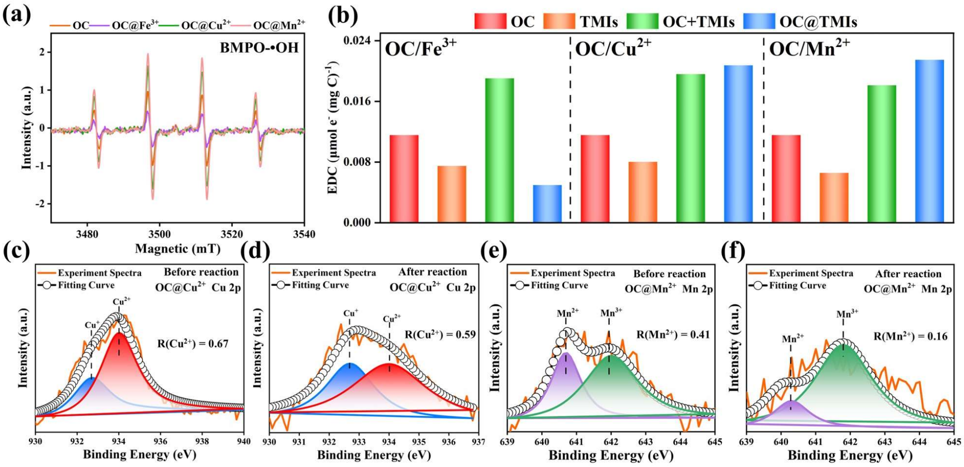

Figure 4. (a) BMPO-•OH adduct EPR spectra of OC, OC@Fe^{3+}, OC@Cu^{2+} and OC@Mn^{2+} under irradiation. (b) Electron donating capacity (EDC) of OC, TMIs, OC+TMIs and OC@TMIs (OC+TMIs denoted the arithmetic sum of the EDC measured for OC and TMIs in separate experiments). High-resolution XPS spectra of Cu 2p for OC@Cu^{2+} (c) before and (d) after the reaction, and Mn 2p for OC@Mn^{2+} (e) before and (f) after the reaction (R(Cu^{2+}) and R(Mn^{2+}) denoted the proportion of Cu^{2+} and Mn^{2+} on the surface, respectively).

As shown in the reaction R3, $•O_2^{-}$ formation relied not only on the photogenerated electrons but also on the O_2 activation. To elucidate the effect of TMIs complexation on the O_2 activation, DFT calculations were carried out in the interaction of O_2 with MS (Fig. S15). Fig. 5a displays that O_2 adsorption energy on MS was −82.03 kJ mol^{-1}, with O−O bond length of 1.20 Å. For MS@Fe^{3+}, O_2 adsorption energy became more negative (−205.59 kJ mol^{-1}), reflecting stronger electrostatic binding due to high positive charge of metal center (Zhang et al., 2024). However, O−O bond length remained unchanged, suggesting negligible electron transfer into the π* antibonding orbital of O_2. Thus, O_2 is strongly bound yet not appreciably activated. Complexation between OC with Cu^{2+} or Mn^{2+} obviously enhanced the adsorption of O_2 (−212.93 kJ mol^{-1} for Cu^{2+} and −366.32 kJ mol^{-1} for Mn^{2+}), but also elongated the O−O bond length to 1.21 Å and 1.32 Å, respectively. These changes suggest electron transfer from the metal centers to the π* antibonding orbital of O_2, boosting effective activation of O_2 and facilitating the $\bullet O_2^-$ generation. Compared to Cu^{2+}, Mn^{2+} exhibited stronger O_2 activation, which was attributed to its half-filled $3d^5$ configuration and moderate redox potential, both of which favored efficient π* electron donation.

Accordingly, Fe^{3+} inhibited electron generation and failed to activate O_2, whereas Cu^{2+} and Mn^{2+} promoted these two processes, with Mn^{2+} showing stronger enhancement effect. This led to the $\bullet O_2^-$ signal intensity of OC@Mn^{2+} > OC@Cu^{2+} > OC > OC@Fe^{3+} (Fig. 5b). $\bullet O_2^-$ directly contributed to H_2O_2 formation (R4), which was quantified with a $TiOSO_4$ chromogenic method (Fig. S16). Fig. 5c shows that H_2O_2 production trend had the consistency with •OH generation ability among these samples (Fig. 4a), which ultimately governed the photoconversion of SO_2 to sulfates.

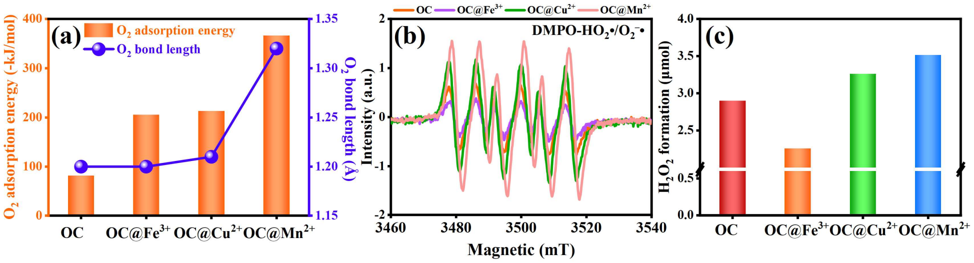

Figure 5. (a) O_2 adsorption energy and the bond length of O_2 for MS, MS@Fe^{3+}, MS@Cu^{2+} and MS@Mn^{2+}. (b) EPR spectra of DMPO-$HO_2\bullet$/$\bullet O_2^-$ adduct for OC, OC@Fe^{3+}, OC@Cu^{2+} and OC@Mn^{2+} under irradiation. (c) H_2O_2 formation from the photochemical reactions on

OC, OC@Fe^{3+}, OC@Cu^{2+} and OC@Mn^{2+}.

4 Conclusions and atmospheric implications

It was well confirmed that the heterogeneous photooxidation of SO_2 to sulfates was strongly modulated by the interactions of OC with TMIs. As evidenced by SO_2 uptake coefficient and sulfate formation mass, Fe^{3+} exhibited a significantly inhibitory effect, whereas Cu^{2+} and Mn^{2+} promoted the conversion of SO_2 to sulfates, with Mn^{2+} playing a more obvious enhancement role. Spectroscopic analyses and DFT calculations consistently demonstrated that Fe^{3+} had the strongest binding affinity to OC chromophores, followed by Cu^{2+} and Mn^{2+}. This difference in the complexation strength controlled the electron generation, O_2 activation, and the sequential formation of $•O_2^-$, H_2O_2, and •OH. The regulation of sulfate formation on OC by TMIs was largely governed by their capacity to suppress or enhance •OH generation.

The photochemical lifetime of SO_2 (τ_{SO_2}) on OC@TMIs was calculated with Eq. (2) (Yang et al., 2021),

$$\tau_{SO_2} = \frac{4}{\gamma \nu A} \quad (2)$$

where γ represents the uptake coefficient of SO_2; ν denotes the mean SO_2 molecular velocity; A corresponds to the aerosol surface area concentration (6.25×10^{-5} cm^2 cm^{-3}) (Liu et al., 2020b; Yang et al., 2021). Under typical atmospheric conditions (40 ppb SO_2, 60% RH), γ_{ss} for SO_2 on OC@TMIs were determined to be $(0.39–22.6) \times 10^{-6}$. If organic matters contributed to 20% of aerosol mass, τ_{SO_2} was estimated to be 5.2–330 days in the coexistence case of OC and TMIs. By contrast, τ_{SO_2} on OC from coal combustion was much narrower, which ranged from 17 to 53 days under the same conditions (Yang et al., 2025).

To assess the atmospheric production of sulfates during the photooxidation of SO_2 on OC@TMIs, the sulfate formation rate (R) was estimated using Eq. (3),

$$R = \frac{d[SO_4^{2-}]}{dt} = \left[\frac{R_P}{D_g} + \frac{4}{\gamma \nu}\right]^{-1} A\,[SO_2] \quad (3)$$

where D_g refers to the diffusion coefficient of SO_2 (1.12×10^{-5} m^2 s^{-1}); R_P denotes the aerosol particle radius and is estimated via Eq. (4) (Li et al., 2020),

$$R_P = \left(0.254 \times \frac{[PM_{2.5}]}{(\mu g\ m^{-3})} + 10.259\right) \times 10^{-9} \quad (4)$$

where $[PM_{2.5}]$ denotes the mean mass concentration of $PM_{2.5}$, and a representative concentration of 300 μg m^{-3} for the polluted episodes in typical Chinese cities was adopted here (Li et al., 2020). Under these conditions, R was determined to be 0.08−4.56 μg m^{-3} h^{-1}, which was a substantially broader range than 0.43−1.33 μg m^{-3} h^{-1} for OC (Yang et al., 2025). Broader ranges of τ_{SO_2} and R on OC@TMIs indicate that the coexistence of OC and TMIs significantly modulates the photochemical conversion of SO_2 to sulfates. These findings suggest that current model simulations may underestimate or overestimate sulfate formation on OC by overlooking such antagonistic or synergistic processes.

It has been well demonstrated that •OH was the dominant active species responsible for the oxidation of SO_2 to sulfates on OC@TMIs (Fig. 4 and S14). Other metal ions (Ca^{2+}, Co^{2+}, Zn^{2+}, Mg^{2+}, Ni^{2+}, Cr^{3+} and Al^{3+}) commonly presenting in atmospheric aerosols were expanded to examine whether this mechanism exhibited broader generality (Hua et al., 2024). As shown in Fig. 6a, the peaks of BMPO-•OH adducts were observed under irradiation, confirming the •OH generation on all OC@TMIs. Relative to OC, the coexistence of Ca^{2+}, Co^{2+}, Zn^{2+} and Mg^{2+} obviously promoted the •OH generation, while Ni^{2+}, Cr^{3+} and Al^{3+} exerted an inhibitory effect. Fig. S17 summarized the mass of sulfates formed on OC@TMIs, which was consistent with the •OH generation trend. Importantly, a linearly positive relationship ($R^2 = 0.95$) between •OH intensity and sulfate mass ($M_{sulfates}$) was determined in Fig. 6b. $M_{sulfates}$ can be parametrized as a function of •OH signal intensity (I) with an Eq.: $M_{sulfates} = (1.23 \pm 0.88) \times 10^{-2} \times I$. This quantitative relationship highlighted the potential dual roles of metal ion types in the sulfate formation, challenging the traditional view that metal ions often promote the SO_2 oxidation (Cao et al., 2024a; Wang et al., 2022; Wang et al., 2021a). It also emphasized the critical role of •OH in the sulfate formation on OC@TMIs. Accordingly, incorporating the •OH generation ability of diverse OC@TMIs complexes into the atmospheric models is essential to accurately constrain sulfate source strength, predict haze evolution and assess associated health impacts in polluted environments.

https://doi.org/10.5194/egusphere-2026-1728
Preprint. Discussion started: 18 May 2026

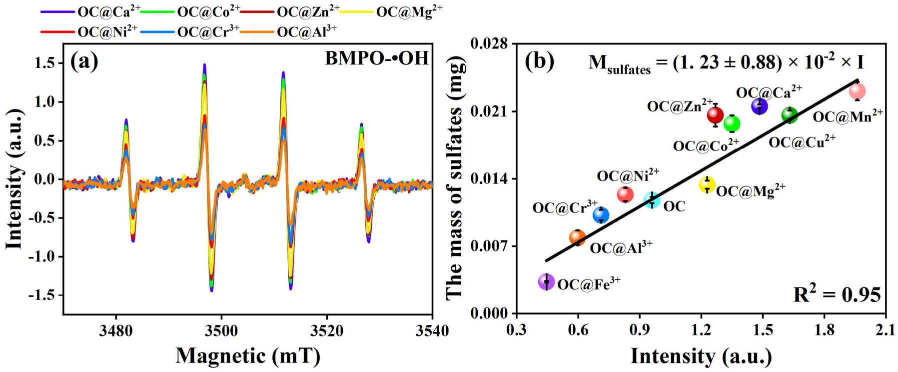

Figure 6. (a) BMPO-•OH adduct EPR spectra. (b) The correlation of $M_{sulfates}$ with the generation of •OH.

Data availability. The data used in this study are available from the corresponding author upon request (hanch@smm.neu.edu.cn).

Supplement. Figures, texts and tables about experimental section, background experiment of SO_2 uptake, complexation evidences of OC with metal ions, the mechanism verification and atmospheric implication.

Author contributions. CH and SY designed the experiment; SY and SL conducted the experiments; SY, SL, JZ, HN, FL and WY performed the data interpretation; CH and SY wrote the paper. CH supervised the project. All authors contributed to the paper with useful scientific.

Competing interests. The contact author has declared that none of the authors has any competing interests.

Financial support. This work has been supported by the National Natural Science Foundation of China (grant nos. 42575113, 42577113, 42077198 and 22206023), and the Fundamental Research Funds for the Central Universities (grant no. N25GFZ016). The characterization analysis of this work was supported by the Analytical and Testing Center of Northeastern University, China.

References

Biesinger, M. C., Payne, B. P., Grosvenor, A. P., Lau, L. W. M., Gerson, A. R., and Smart, R. S. C.: Resolving surface chemical states in XPS analysis of first row transition metals, oxides and hydroxides: Cr, Mn, Fe, Co and Ni, Appl. Surf. Sci., 257, 2717−2730, https://doi.org/10.1016/j.apsusc.2010.10.051, 2011.

Cao, X., Liu, Y.-X., Huang, Q., Chen, Z., Sun, J., Sun, J., Pang, S.-F., Liu, P., Wang, W., Zhang, Y.-H., and Ge, M.: Single droplet tweezer revealing the reaction mechanism of Mn(II)-catalyzed SO_2 oxidation, Environ. Sci. Technol., 58, 5068−5078, https://doi.org/10.1021/acs.est.4c00309, 2024a.

Cao, Y., Liu, J., Ma, Q., Zhang, C., Zhang, P., Chen, T., Wang, Y., Chu, B., Zhang, X., Francisco, J. S., and He, H.: Photoactivation of chlorine and its catalytic role in the formation of sulfate aerosols, J. Am. Chem. Soc., 146, 1467−1475, https://doi.org/10.1021/jacs.3c10840, 2024b.

Cerrato, J. M., Hochella, M. F., Jr., Knocke, W. R., Dietrich, A. M., and Cromer, T. F.: Use of XPS to identify the oxidation state of Mn in solid surfaces of filtration media oxide samples from drinking water treatment plants, Environ. Sci. Technol., 44, 5881−5886, https://doi.org/10.1021/es100547q, 2010.

Cheng, Y., Zheng, G., Wei, C., Mu, Q., Zheng, B., Wang, Z., Gao, M., Zhang, Q., He, K., Carmichael, G., Pöschl, U., and Su, H.: Reactive nitrogen chemistry in aerosol water as a source of sulfate during haze events in China, Sci. Adv., 2, e1601530, https://doi.org/10.1126/sciadv.1601530, 2016.

Deng, J., Ma, H., Wang, X., Zhong, S., Zhang, Z., Zhu, J., Fan, Y., Hu, W., Wu, L., Li, X., Ren, L., Pavuluri, C. M., Pan, X., Sun, Y., Wang, Z., Kawamura, K., and Fu, P.: Measurement report: Optical properties and sources of water-soluble brown carbon in Tianjin, North China-insights from organic molecular compositions, Atmos. Chem. Phys. 22, 6449−6470, https://doi.org/10.5194/acp-22-6449-2022, 2022.

Dupart, Y., King, S. M., Nekat, B., Nowak, A., Wiedensohler, A., Herrmann, H., David, G., Thomas, B., Miffre, A., Rairoux, P., D'Anna, B., and George, C.: Mineral dust photochemistry induces nucleation events in the presence of SO_2, P. Natl. Acad. Sci. USA, 109, 20842−20847, https://doi.org/10.1073/pnas.1212297109, 2012.

Eckhardt, S., Quennehen, B., Olivié, D. J. L., Berntsen, T. K., Cherian, R., Christensen, J. H., Collins, W., Crepinsek, S., Daskalakis, N., Flanner, M., Herber, A., Heyes, C., Hodnebrog, Ø., Huang, L., Kanakidou, M., Klimont, Z., Langner, J., Law, K. S., Lund, M. T., Mahmood, R., Massling, A., Myriokefalitakis, S., Nielsen, I. E., Nøjgaard, J. K., Quaas, J., Quinn, P. K., Raut, J. C., Rumbold, S. T., Schulz, M., Sharma, S., Skeie, R. B., Skov, H., Uttal, T., von Salzen, K., and Stohl, A.: Current model capabilities for simulating black carbon and sulfate concentrations in the Arctic atmosphere: A multi-model evaluation using a comprehensive measurement data set, Atmos. Chem. Phys., 15, 9413–9433, https://doi.org/10.5194/acp-15-9413-2015, 2015.

Fan, X., Wei, S., Zhu, M., Song, J., and Peng, P. a.: Comprehensive characterization of humic-like substances in smoke $PM_{2.5}$ emitted from the combustion of biomass materials and fossil fuels, Atmos. Chem. Phys., 16, 13321–13340, https://doi.org/10.5194/acp-16-13321-2016, 2016.

Fulda, B., Voegelin, A., Maurer, F., Christl, I., and Kretzschmar, R.: Copper redox transformation and complexation by reduced and oxidized soil humic acid. 1. X-ray absorption spectroscopy study, Environ. Sci. Technol., 47, 10903–10911, https://doi.org/10.1021/es4024089, 2013.

Hansard, S. P., Easter, H. D., and Voelker, B. M.: Rapid Reaction of Nanomolar Mn(II) with Superoxide Radical in Seawater and Simulated Freshwater, Environ. Sci. Technol., 45, 2811–2817, https://doi.org/10.1021/es104014s, 2011.

Hoyle, C. R., Fuchs, C., Järvinen, E., Saathoff, H., Dias, A., El Haddad, I., Gysel, M., Coburn, S. C., Tröstl, J., Bernhammer, A. K., Bianchi, F., Breitenlechner, M., Corbin, J. C., Craven, J., Donahue, N. M., Duplissy, J., Ehrhart, S., Frege, C., Gordon, H., Höppel, N., Heinritzi, M., Kristensen, T. B., Molteni, U., Nichman, L., Pinterich, T., Prévôt, A. S. H., Simon, M., Slowik, J. G., Steiner, G., Tomé, A., Vogel, A. L., Volkamer, R., Wagner, A. C., Wagner, R., Wexler, A. S., Williamson, C., Winkler, P. M., Yan, C., Amorim, A., Dommen, J., Curtius, J., Gallagher, M. W., Flagan, R. C., Hansel, A., Kirkby, J., Kulmala, M., Möhler, O., Stratmann, F., Worsnop, D. R., and Baltensperger, U.: Aqueous phase oxidation of sulphur dioxide by ozone in cloud droplets, Atmos. Chem. Phys., 16, 1693–1712, https://doi.org/10.5194/acp-16-1693-2016, 2016.

Hua, C., Ma, W., Zheng, F., Zhang, Y., Xie, J., Ma, L., Song, B., Yan, C., Li, H., Liu, Z., Liu, Q., Kulmala, M., and Liu, Y.: Health risks and sources of trace elements and black carbon in

$PM_{2.5}$ from 2019 to 2021 in Beijing, J. Environ. Sci., 142, 69–82, https://doi.org/10.1016/j.jes.2023.05.023, 2024.

Hua, C., Ma, W., Li, J., Wang, Y., Zheng, F., Zhang, Y., Ren, Y., Chen, T., Li, H., Bianchi, F., Petaja, T., Kerminen, V. M., Worsnop, D., Kulmala, M., Kan, H., and Liu, Y.: Internal exposure risks of particle-bound polycyclic aromatic hydrocarbons with an hourly time resolution to humans in Beijing, Environ. Sci. Technol., 59, 12035–12047, https://doi.org/10.1021/acs.est.5c00578, 2025.

Huang, R.-J., Zhang, Y., Bozzetti, C., Ho, K.-F., Cao, J.-J., Han, Y., Daellenbach, K. R., Slowik, J. G., Platt, S. M., Canonaco, F., Zotter, P., Wolf, R., Pieber, S. M., Bruns, E. A., Crippa, M., Ciarelli, G., Piazzalunga, A., Schwikowski, M., Abbaszade, G., Schnelle-Kreis, J., Zimmermann, R., An, Z., Szidat, S., Baltensperger, U., Haddad, I. E., and Prévôt, A. S. H.: High secondary aerosol contribution to particulate pollution during haze events in China, Nature, 514, 218–222, https://doi.org/10.1038/nature13774, 2014.

Jiang, S.-d., Wang, Z.-h., Zhou, J.-h., Wen, Z.-c., and Cen, K.-f.: A quantum chemistry study on reaction mechanisms of SO_2 with O_3 and H_2O_2, J. Zhejiang Univ-Sci. A, 10, 1327–1333, https://doi.org/10.1631/jzus.A0820787, 2009.

Kuramochi, Y., Ishitani, O., and Ishida, H.: Reaction mechanisms of catalytic photochemical CO_2 reduction using Re(I) and Ru(II) complexes, Coord. Chem. Rev., 373, 333–356, https://doi.org/10.1016/j.ccr.2017.11.023, 2018.

Li, G., Bei, N., Cao, J., Huang, R., Wu, J., Feng, T., Wang, Y., Liu, S., Zhang, Q., Tie, X., and Molina, L. T.: A possible pathway for rapid growth of sulfate during haze days in China, Atmos. Chem. Phys., 17, 3301–3316, https://doi.org/10.5194/acp-17-3301-2017, 2017.

Li, H., Santos, F., Butler, K., and Herndon, E.: A critical review on the multiple roles of manganese in stabilizing and destabilizing soil organic matter, Environ. Sci. Technol., 55, 12136–12152, https://doi.org/10.1021/acs.est.1c00299, 2021.

Li, H., Yang, K., Hai, L., Wang, Z., Luo, Y., He, L., Yi, W., Li, J., Xu, C., Deng, L., and He, D.: Photothermal-triggered release of alkyl radicals and cascade generation of hydroxyl radicals via a versatile hybrid nanocatalyst for hypoxia-irrelevant synergistic antibiofilm therapy, Chem. Eng. J., 455, 140903, https://doi.org/10.1016/j.cej.2022.140903, 2023.

Li, J., Chen, Q., Sha, T., and Liu, Y.: Significant promotion of light absorption ability and formation of triplet organics and reactive oxygen species in atmospheric HULIS by Fe(III) ions, Environ. Sci. Technol., 56, 16652−16664, https://doi.org/10.1021/acs.est.2c05137, 2022.

Li, J., Zhang, Y.-L., Cao, F., Zhang, W., Fan, M., Lee, X., and Michalski, G.: Stable sulfur isotopes revealed a major role of transition-metal ion-catalyzed SO_2 oxidation in haze episodes, Environ. Sci. Technol., 54, 2626−2634, https://doi.org/10.1021/acs.est.9b07150, 2020.

Liu, J., Li, X., Chu, Y., Yuan, L., Lv, R., and Zhang, W.: An autocatalytic Fe(III)/H_2O_2 Fenton-like process triggered by tetracycline: The overlooked effect of quinone intermediates, Chem. Eng. J., 475, 146035, https://doi.org/10.1016/j.cej.2023.146035, 2023.

Liu, T. and Abbatt, J. P. D.: Oxidation of sulfur dioxide by nitrogen dioxide accelerated at the interface of deliquesced aerosol particles, Nat. Chem., 13, 1173−1177, https://doi.org/10.1038/s41557-021-00777-0, 2021.

Liu, T., Clegg, S. L., and Abbatt, J. P. D.: Fast oxidation of sulfur dioxide by hydrogen peroxide in deliquesced aerosol particles, P. Natl. Acad. Sci. USA, 117, 1354−1359, https://doi.org/10.1073/pnas.1916401117, 2020a.

Liu, X., Lu, J., Fang, X., Zhou, J., and Chen, Q.: Complexation modelling and oxidation mechanism of organic pollutants in cotton pulp black liquor during iron salt precipitation and electrochemical treatment, Chemosphere, 308, 136374, https://doi.org/10.1016/j.chemosphere.2022.136374, 2022.

Liu, Y., Zhao, W., Zhang, P., Fu, Q.-l., Yu, C., and Yuan, S.: Asymmetrical changes of electron-donating and electron-accepting capacities of natural organic matter during its interaction with Fe oxyhydroxides, Chem. Geol., 661, 122189, https://doi.org/10.1016/j.chemgeo.2024.122189, 2024.

Liu, Y., Wang, T., Fang, X., Deng, Y., Cheng, H., Bacha, A.-U.-R., Nabi, I., and Zhang, L.: Brown carbon: An underlying driving force for rapid atmospheric sulfate formation and haze event, Sci. Total Environ., 734, 139415, https://doi.org/10.1016/j.scitotenv.2020.139415, 2020b.

Lu, S., Win, M. S., Zeng, J., Yao, C., Zhao, M., Xiu, G., Lin, Y., Xie, T., Dai, Y., Rao, L., Zhang, L., Yonemochi, S., and Wang, Q.: A characterization of HULIS-C and the oxidative potential of HULIS and HULIS-Fe(II) mixture in $PM_{2.5}$ during hazy and non-hazy days in Shanghai, Atmos. Environ., 219, 117058, https://doi.org/10.1016/j.atmosenv.2019.117058, 2019.

Lu, T.: A comprehensive electron wavefunction analysis toolbox for chemists, Multiwfn, J. Chem. Phys., 161, 082503, https://doi.org/10.1063/5.0216272, 2024.

Lu, T. and Chen, F.: Multiwfn: A multifunctional wavefunction analyzer, J. Comput. Chem., 33, 580−592, https://doi.org/10.1002/jcc.22885, 2011.

Ma, W., He, J., Han, L., Ma, C., Cai, Y., Guo, X., and Yang, Z.: Hydrophilic fraction of dissolved organic matter largely facilitated microplastics photoaging: Insights from redox properties and reactive oxygen species, Environ. Sci. Technol., 58, 11625−11636, https://doi.org/10.1021/acs.est.3c11111, 2024.

Nørskov, J. K., Rossmeisl, J., Logadottir, A., Lindqvist, L., Kitchin, J. R., Bligaard, T., and Jónsson, H.: Origin of the overpotential for oxygen reduction at a fuel-cell cathode, J. Phys. Chem. B, 108, 17886−17892, https://doi.org/10.1021/jp047349j, 2004.

Pan, Y., Ruan, X., Garg, S., Waite, T. D., Lei, Y., and Yang, X.: Copper inhibition of triplet-sensitized phototransformation of phenolic and amine contaminants, Environ. Sci. Technol., 54, 9980−9989, https://doi.org/10.1021/acs.est.0c01693, 2020.

Peng, J., Hu, M., Shang, D., Wu, Z., Du, Z., Tan, T., Wang, Y., Zhang, F., and Zhang, R.: Explosive secondary aerosol formation during severe haze in the North China Plain, Environ. Sci. Technol., 55, 2189−2207, https://doi.org/10.1021/acs.est.0c07204, 2021.

Ruzi, R., Zhang, M., Ablajan, K., and Zhu, C.: Photoredox-catalyzed deoxygenative intramolecular acylation of biarylcarboxylic acids: Access to fluorenones, J. Org. Chem., 82, 12834−12839, https://doi.org/10.1021/acs.joc.7b02197, 2017.

Salana, S., Yu, H., Dai, Z., Subramanian, P. S. G., Puthussery, J. V., Wang, Y., Singh, A., Pope, F. D., Leiva, G. M., Rastogi, N., Tripathi, S. N., Weber, R. J., and Verma, V.: Inter-continental variability in the relationship of oxidative potential and cytotoxicity with $PM_{2.5}$ mass, Nat. Commun., 15, 5263, https://doi.org/10.1038/s41467-024-49649-4, 2024.

Shiraiwa, M., Li, Y., Tsimpidi, A. P., Karydis, V. A., Berkemeier, T., Pandis, S. N., Lelieveld, J., Koop, T., and Pöschl, U.: Global distribution of particle phase state in atmospheric secondary organic aerosols, Nat. Commun., 8, 15002, https://doi.org/10.1038/ncomms15002, 2017.

Tang, R., Zhang, R., Ma, J., Song, K., Mabato, B. R. G., Cuevas, R. A. I., Zhou, L., Liang, Z., Vogel, A. L., Guo, S., and Chan, C. K.: Sulfate formation by photosensitization in mixed incense burning–sodium chloride particles: Effects of RH, light intensity, and aerosol aging, Environ. Sci. Technol., 57, 10295−10307, https://doi.org/10.1021/acs.est.3c02225, 2023.

Treacy, S. M. and Rovis, T.: Photoinduced ligand-to-metal charge transfer in base-metal catalysis, Synthesis, 56, 1967−1978, https://doi.org/10.1055/s-0042-1751518, 2024.

Tsona, N. T. and Du, L.: A potential source of atmospheric sulfate from O_2^--induced SO_2 oxidation by ozone, Atmos. Chem. Phys., 19, 649−661, https://doi.org/10.5194/acp-19-649-2019, 2019.

Wan, D., Sharma, V. K., Liu, L., Zuo, Y., and Chen, Y.: Mechanistic Insight into the effect of metal ions on photogeneration of reactive species from dissolved organic matter, Environ. Sci. Technol., 53, 5778−5786, https://doi.org/10.1021/acs.est.9b00538, 2019.

Wang, T., Liu, M., Liu, M., Song, Y., Xu, Z., Shang, F., Huang, X., Liao, W., Wang, W., Ge, M., Cao, J., Hu, J., Tang, G., Pan, Y., Hu, M., and Zhu, T.: Sulfate formation apportionment during winter haze events in North China, Environ. Sci. Technol., 56, 7771−7778, https://doi.org/10.1021/acs.est.2c02533, 2022.

Wang, W., Liu, Y., Wang, T., Ge, Q., Li, K., Liu, J., You, W., Wang, L., Xie, L., Fu, H., Chen, J., and Zhang, L.: Significantly accelerated photosensitized formation of atmospheric sulfate at the air-water interface of microdroplets, J. Am. Chem. Soc., 146, 6580−6590, https://doi.org/10.1021/jacs.3c11892, 2024.

Wang, W., Liu, M., Wang, T., Song, Y., Zhou, L., Cao, J., Hu, J., Tang, G., Chen, Z., Li, Z., Xu, Z., Peng, C., Lian, C., Chen, Y., Pan, Y., Zhang, Y., Sun, Y., Li, W., Zhu, T., Tian, H., and Ge, M.: Sulfate formation is dominated by manganese-catalyzed oxidation of SO_2 on aerosol surfaces during haze events, Nat. Commun., 12, 1993, https://doi.org/10.1038/s41467-021-22091-6, 2021a.

Wang, X., Qin, Y., Qin, J., Long, X., Qi, T., Chen, R., Xiao, K., and Tan, J.: Spectroscopic insight into the pH-dependent interactions between atmospheric heavy metals (Cu and Zn) and water-soluble organic compounds in $PM_{2.5}$, Sci. Total Environ., 767, 145261, https://doi.org/10.1016/j.scitotenv.2021.145261, 2021b.

Wang, X., Qin, Y., Qin, J., Yang, Y., Qi, T., Chen, R., Tan, J., and Xiao, K.: The interaction laws of atmospheric heavy metal ions and water-soluble organic compounds in $PM_{2.5}$ based on the excitation-emission matrix fluorescence spectroscopy, J. Hazard. Mater., 402, 123497, https://doi.org/10.1016/j.jhazmat.2020.123497, 2021c.

Wang, X., Gemayel, R., Hayeck, N., Perrier, S., Charbonnel, N., Xu, C., Chen, H., Zhu, C., Zhang, L., Wang, L., Nizkorodov, S. A., Wang, X., Wang, Z., Wang, T., Mellouki, A., Riva, M., Chen, J., and George, C.: Atmospheric photosensitization: A new pathway for sulfate formation, Environ. Sci. Technol., 54, 3114−3120, https://doi.org/10.1021/acs.est.9b06347, 2020.

Wang, Y., Zhang, Q., Jiang, J., Zhou, W., Wang, B., He, K., Duan, F., Zhang, Q., Philip, S., and Xie, Y.: Enhanced sulfate formation during China's severe winter haze episode in January 2013 missing from current models, J. Geophys. Res.-Atmos., 119, 10425−10440, https://doi.org/10.1002/2013JD021426, 2014.

Xing, X., Li, Z., Wang, Y., Tian, Z., Liu, D., Cheng, J., and Hao, Z.: Synergistic catalytic degradation of benzene and toluene on spinel MMn_2O_4 (MCo, Ni, Cu) catalysts, J. Environ. Sci., 154, 238−251, https://doi.org/10.1016/j.jes.2024.08.016, 2025.

Yang, H., Yang, W., Ma, J., and Han, C.: Heterogeneous photochemical uptake of SO_2 on typical brown carbon species: A significant sulfate source, Atmos. Environ., 324, 120425, https://doi.org/10.1016/j.atmosenv.2024.120425, 2024a.

Yang, S., Yang, H., Na, H., Zheng, J., Yang, W., and Han, C.: Quantitative relationships between physicochemical properties of organic carbon from coal combustion and heterogeneous photooxidation of SO_2 to sulfates, J. Hazard. Mater., 495, 139132, https://doi.org/10.1016/j.jhazmat.2025.139132, 2025.

Yang, W., Zhang, T., Han, C., Tang, N., Yang, H., and Xue, X.: Photoenhanced heterogeneous reaction of O_3 with humic acid: Focus on O_3 uptake and changes in the composition and optical property, Environ. Pollut., 268, 115696, https://doi.org/10.1016/j.envpol.2020.115696, 2021.

Yang, W., Xia, Z., Zheng, J., Li, F., Nan, X., Du, T., and Han, C.: Reactive oxygen species play key roles in the nitrite formation by the inorganic nitrate photolysis in the presence of urban water-soluble organic carbon, Sci. Total Environ., 946, 174203, https://doi.org/10.1016/j.scitotenv.2024.174203, 2024b.

Zhang, F., Wang, Y., Peng, J., Chen, L., Sun, Y., Duan, L., Ge, X., Li, Y., Zhao, J., Liu, C., Zhang, X., Zhang, G., Pan, Y., Wang, Y., Zhang, A. L., Ji, Y., Wang, G., Hu, M., Molina, M. J., and Zhang, R.: An unexpected catalyst dominates formation and radiative forcing of regional haze, P. Natl. Acad. Sci. USA, 117, 3960–3966, https://doi.org/10.1073/pnas.1919343117, 2020a.

Zhang, P., Chen, T., Ma, Q., Chu, B., Wang, Y., Mu, Y., Yu, Y., and He, H.: Diesel soot photooxidation enhances the heterogeneous formation of H_2SO_4, Nat. Commun., 13, 5364, https://doi.org/10.1038/s41467-022-33120-3, 2022.

Zhang, P., Wang, Y., Chen, T., Yu, Y., Ma, Q., Liu, C., Li, H., Chu, B., and He, H.: Insight into the mechanism and kinetics of the heterogeneous reaction between SO_2 and NO_2 on diesel black carbon under light irradiation, Environ. Sci. Technol., 57, 17718–17726, https://doi.org/10.1021/acs.est.2c09674, 2023.

Zhang, P., Chen, H. C., Zhu, H., Chen, K., Li, T., Zhao, Y., Li, J., Hu, R., Huang, S., Zhu, W., Liu, Y., and Pan, Y.: Inter-site structural heterogeneity induction of single atom Fe catalysts for robust oxygen reduction, Nat. Commun., 15, 2062, https://doi.org/10.1038/s41467-024-46389-3, 2024.

Zhang, Q., Shen, Z., Zhang, L., Zeng, Y., Ning, Z., Zhang, T., Lei, Y., Wang, Q., Li, G., Sun, J., Westerdahl, D., Xu, H., and Cao, J.: Investigation of primary and secondary particulate brown carbon in two chinese cities of Xi'an and Hong Kong in wintertime, Environ. Sci. Technol., 54, 3803–3813, https://doi.org/10.1021/acs.est.9b05332, 2020b.

Zhang, R. and Chan, C. K.: Simultaneous formation of sulfate and nitrate via co-uptake of SO_2 and NO_2 by aqueous NaCl droplets: Combined effect of nitrate photolysis and chlorine chemistry, Atmos. Chem. Phys., 23, 6113–6126, https://doi.org/10.5194/acp-23-6113-2023, 2023.

Zhang, Y., Bao, F., Li, M., Chen, C., and Zhao, J.: Nitrate-enhanced oxidation of SO_2 on mineral dust: A vital role of a proton, Environ. Sci. Technol., 53, 10139–10145, https://doi.org/10.1021/acs.est.9b01921, 2019.

Zhang, Y., Bao, F., Li, M., Xia, H., Huang, D., Chen, C., and Zhao, J.: Photoinduced uptake and oxidation of SO_2 on Beijing urban $PM_{2.5}$, Environ. Sci. Technol., 54, 14868–14876, https://doi.org/10.1021/acs.est.0c01532, 2020c.

https://doi.org/10.5194/egusphere-2026-1728
Preprint. Discussion started: 18 May 2026

Zheng, B., Zhang, Q., Zhang, Y., He, K. B., Wang, K., Zheng, G. J., Duan, F. K., Ma, Y. L., and Kimoto, T.: Heterogeneous chemistry: A mechanism missing in current models to explain secondary inorganic aerosol formation during the January 2013 haze episode in North China, Atmos. Chem. Phys., 15, 2031–2049, https://doi.org/10.5194/acp-15-2031-2015, 2015.

Zhu, J., Sheng, M., Shang, J., Kuang, Y., Shi, X., and Qiu, X.: Photocatalytic role of atmospheric soot particles under visible-light irradiation: Reactive oxygen species generation, self-oxidation process, and induced higher oxidative potential and cytotoxicity, Environ. Sci. Technol., 56, 7668–7678, https://doi.org/10.1021/acs.est.2c00420, 2022.